Appl Phys B (2010) 98: 711–721
DOI 10.1007/s00340-009-3707-5

Applied Physics B
Lasers and Optics

Theory of laser ion acceleration from a foil target of nanometer thickness

X.Q. Yan · T. Tajima · M. Hegelich · L. Yin · D. Habs

Received: 24 July 2009 / Revised version: 30 July 2009 / Published online: 16 September 2009

Abstract A theory for ion acceleration by ultrashort laser pulses is presented to evaluate the maximum ion energy in the interaction of ultrahigh contrast (UHC) intense laser pulses with a nanometer-scale foil. In this regime, the ion energy may be directly related to the laser intensity and subsequent electron dynamics. This leads to a simple analytical expression for the ion energy gain under the laser irradiation of thin targets. Significantly higher energies for thin targets than for thicker targets are predicted. The theory is concretized with a view to compare with the results and their details of recent experiments.

PACS 52.59.-f · 52.38.Kd · 52.35.Mw

X.Q. Yan (✉) · D. Habs
Max-Planck-Institut f. Quantenoptik, 85748 Garching, Germany
e-mail: xyan@mpq.mpg.de
e-mail: x.yan@pku.edu.cn

X.Q. Yan
State Key Lab of Nuclear Physics and Technology, Peking University, Beijing 100871, China

X.Q. Yan
Center for Applied Physics and Technology, Peking University, Beijing, China

T. Tajima
Photo-Medical Research Center, JAEA, Kyoto 619-0215, Japan

T. Tajima · M. Hegelich · D. Habs
Fakultaet f. Physik, LMU Muenchen, 85748 Garching, Germany

M. Hegelich · L. Yin
Los Alamos National Laboratory, Los Alamos, NM 87545, USA

1 Introduction

The dream of collective acceleration started with the vision of Veksler [1] and Budker [2]. If ions were to be trapped by speeding electron cloud or beam with energy ε_e, the ions would be accelerated to the energy of $\varepsilon_i = (M/m)\varepsilon_e$, where M and m are the masses of ions and electrons, respectively, because they would speed with the same velocity. Since the mass ratio M/m of ions to electrons is nearly 2000 for protons and greater for other ions, the collective acceleration of ions would gain a large energy boost. A large body of investigations ensued [3–5]. Also started were investigations of electron clouds to cool and/or accelerate ions in storage rings or traps as a variation of this vision (see, e.g. [6]). In this the electron cloud slightly ahead of the ion beam with some velocity differential can cause a frictional force of the Bethe-Bloch type to drag ions for acceleration and/or cooling, if and when the velocity difference between electrons and ions is controlled under the given condition (an 'adiabatic' condition). The friction force arising from the electron bunch here plays a role similar to the friction played by photon pressure on atoms in the case of the work of Chu [7]. None of the collective acceleration experiments, however, found energy enhancement of the magnitude mentioned above. The primary reason for this was attributed to the sluggishness (inertia) of ions and the electrons being pulled back to ions, instead of the other way around, too fast 'reflexing of electrons' as described in [8]. In other words, the fast dynamics of light electrons is mismatched with the slow dynamics of heavy ions. As we shall see in more detail, Mako and Tajima theoretically found that the ion energy may be enhanced only by a factor of $2\alpha + 1$ (which is about 6 or 7 for typical experimental situations, and α will be defined later in Sect. 2) over the electron energy, instead of by a factor of nearly 2000, due to the electron reflexing. (For

example, Tajima and Mako [9] suggested one to reduce the culpable electron reflexing by providing a concave geometry.) In the year 2000 the first experiments [10–13] to collectively accelerate ions by laser irradiation were reported. Since then, a large amount of efforts have been steadily dedicated to this subject. We revisit some of these electron dynamics in some detail and analyze subsequent ion dynamics under these electron dynamics.

Because of the advantage in accelerating limited mass by a laser to cope with the mismatch between the electron and ion dynamics as discussed above, experiments producing high-energy ions from sub-micrometer to nanometer targets much thinner than the ones in early experiments driven by ultrahigh contrast (UHC) short-pulse lasers [14–18] have recently attracted strong interest. Of particular focus is how much the ion energy enhancement is observed in the experiments and simulations in these thin targets and how it scales with the laser intensity.

The experiments and simulations of late show that the proton energy increases as the target thickness decreases for a given laser intensity, and that there is an optimal thickness of the target (at several nm) at which the maximum proton energy peaks and below which the proton energy now decreases. This optimal thickness for the peak proton energy is consistent with the thickness dictated by the relation $a_0 \sim \sigma = \frac{n_0}{n_c}\frac{d}{\lambda}$, where σ is the (dimensionless) normalized electron areal density, a_0 and d are the (dimensionless) normalized amplitude of electric field of laser and target thickness [19–24]. This is understood as arising from the condition that the radiation force pushes out electrons from the foil layer if $\sigma \leq a_0$ or $\xi \leq 1$, while with $\sigma \geq a_0$ or $\xi \geq 1$ the laser pulse does not have sufficient power to cause maximal polarization to all electrons. Here we have introduced the dimensionless parameter of the ratio of the normalized areal density to the normalized laser amplitude $\xi = \sigma/a_0$. Note that this optimal thickness for a typical available laser intensity is way smaller than for cases with previously attempted target thicknesses (for ion acceleration). Thus we attribute the observed singularly large value of the maximum proton energy in the recent experiment [25] to the ability to identify and provide prepared thin targets on the order of nm to reach this optimal condition. In reality at this target thickness the laser field teeters over partial penetration through the target, rendering the realization of the optimum rather sensitive. Under this condition, electron motions maintain primarily those organized characteristics directly influenced by the laser field, rather than chaotic and thermal motions of electrons resulting from laser heating. In 1D3V Particle In Cell (PIC) simulation (Fig. 1) we observe that the momenta of the electrons show in fact coherent patterns directed either to the ponderomotive potential direction, the backward electrostatic pull direction, or the wave trapping motion direction, in stark contrast to the broad momenta of thermal

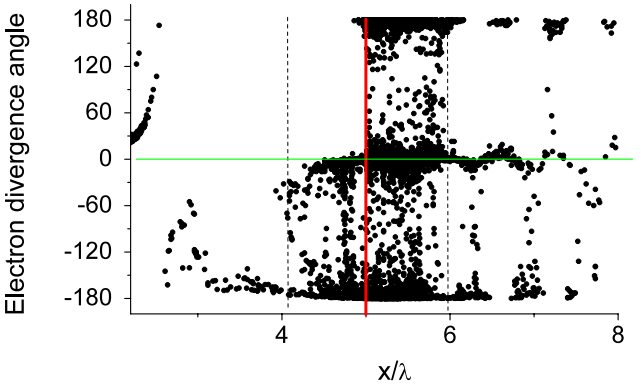

Fig. 1 Coherent electron motions in the laser irradiation on a thin target in 1D3V PIC simulations. The electron divergence angle $\tan^{-1}(p_y/p_x)$ versus position x at $t = 22$, where space x is measured in the wavelength λ and is in the direction of laser propagation and y is the polarization direction, while time t is normalized by the laser cycle. On the left of the target we see electrons backwardly spewed out near an angle of $-180°$. In the forward direction we see forward electrons at 0° due to the ponderomotive force, and electrons reflexing by the electrostatic fields (180° or $-180°$). We further see electrons trapped in some wavelike structure, changing swiftly their directions. All these are indicative of the direct imprint of the electron motion in the laser fields. Note also that even within the target we discern structured electron loci, showing electrons driven by some minute structured (perhaps the wavelength of $2\pi c/\omega_p$) fields in the target. (Laser amplitude $a_0 = 3.6$, $\xi \sim 1$ and normal incidence. The *vertical bold line* represents the initial target located at $x = 5\lambda$, the *two dotted lines* show the boundaries of the expanded target)

electrons. In other words, through a very thin target the partially penetrated laser fields enable the electrons to execute dynamic motions still directly tied with the laser rather than thermal motions. We note that the ponderomotive force due to this trapped radiation contributes to the acceleration of electrons in this sheet and thus retards these electrons from being decelerated by the electrostatic force emanated from the diamond foil. In a typical sheath acceleration scheme the termination of ion acceleration commences due to this electron reflexing by the electrostatic field.

On the other hand, most of the theories have been based on the so-called Plasma Expansion Model (PEM) [26], which is motivated by a much thicker and more massive target. In this regime electrons are first accelerated by the impinging relativistic laser pulse and penetrate the target driven by ponderomotive force. Leaving the target at the rear side, electrons set up an electrostatic field that is pointed normal to the target rear surface, which is the so-called TNSA (Target Normal Sheath Acceleration) acceleration. Most electrons are forced to turn around and build up a quasistationary electron layer. These fast electrons are assumed to follow the thermal or Boltzmann distribution in theoretical studies of the conventional TNSA mechanism for thicker targets [14, 26–28], where the acceleration field is estimated by the exponential potential dependency in the Poisson equation. Though this mechanism is widely used in the interpretation

of the experimental results, it does not apply to the ultrathin nanometer-scale targets, because the direct laser field and attenuated partially transmitted laser pulse play an important role in the electron dynamics and the energetic electrons oscillate coherently, instead of chaotic thermal motions. Based on a self-consistent solution of the Poisson equation and TNSA model, Andreev et al. [14] had proposed an analytical model for thin foils and predicted that the optimum target thickness is about 100 nm. It obviously does not explain the experimental results [25].

In Sects. 2 and 3 we formulate the dynamic treatment of electrons and ions, respectively, coupled through the electrostatic potential self-consistently for laser irradiated ion acceleration from a thin target. In Sect. 4 we discuss the physical effects other than the direct imprints of laser fields on particles after the laser goes through the target. In Sect. 5 we consider physical processes that become relevant when the target is thicker ($\xi \gg 1$), but not on a scale of thickness in the conventional TNSA. In Sect. 6 two classes of simulation results are given to underscore the theoretical model. In Sect. 7 we make our conclusions.

2 Electrostatic potential in coherent dynamics

We formulate the maximal ion energies in the laser driven foil interaction of our regime in this paper, without assuming thermalized electrons. When the foil is thick with $\xi \gg 1$ and the laser pulse is completely reflected, the ion acceleration may be described by the plasma expansion model for thicker targets [26]. On the contrary, in case of $\xi \ll 1$, the transmission is dominant and the laser passes without too much interaction with the target. However, we will note that there is a regime ($\xi \gg 1$) with thickness still much smaller than that for TNSA for thicker targets (to be discussed in Sect. 5). The optimum ion acceleration condition is, as discussed, in the range of $\xi \sim 1$ ($0.1 < \xi < 10$). There appears to be a partially transmitted laser pulse and behind the target energetic electrons still execute the collective motions in the laser field. Electrons quiver with the laser field and are also being pushed forward by the ponderomotive force. We see in Fig. 1 that in the region ahead of the exploding thin target, there are three components of characteristics orbits: a set of orbits in forward direction with angle 0°), the second backward (with −180° or 180°), and the third with loci with curved loops. The first two are characteristics observed even in a simple sheath, but also present in the current case, where perhaps the forward one is as vigorous or more so as the backward one. The third category belongs to the orbits of trapped particles in the laser field or the ponderomotive potential. For a reflexing electron cloud the distribution shows only two components, the forward one and the backward one.

In an ultrathin target, the laser electromagnetic fields largely sustain coherent motions of electrons. As there are partially penetrating laser fields in addition to the laser fields in the target, the electron motion under laser fields is intact and is characterized by the transverse field. The electron energy consists of two contributions, the kinetic energy of (organized) electrons under the laser and the ponderomotive potential of the partially penetrated laser fields that help sustain the electron's forward momentum. We discuss these aspects in more detail in Sect. 4. Following the analysis of Mako and Tajima [8], the plasma density can be determined by

$$n_e = 2\int_0^{V_{\max}} g(V_x)\, dV_x, \tag{1}$$

$$V_{\max} = c\sqrt{1 - m_e^2 c^4/\left(E_0 + m_e c^2\right)^2}, \tag{2}$$

where g is the electron distribution function and E_0 is the maximum electron energy in this theoretical distribution and we call this the characteristic electron energy from now on.

The forward current density of electrons J and electron density n_e are related through

$$J(\upsilon) = -e\int_{\upsilon}^{V_{\max}} V_x g\, dV_x, \tag{3}$$

$$n_e = \frac{2}{e}\int_0^{V_{\max}} \frac{dJ/d\upsilon}{\upsilon}\, d\upsilon. \tag{4}$$

At a given position in the reflexing electron cloud where the potential is ϕ, the total particle energy (disregarding the rest mass energy) is given by

$$E = (\gamma - 1)m_e c^2 - e\phi. \tag{5}$$

The current density can be determined from the 1D simulation results. We find that the current density dependence on E is not exponential, but is rather well fitted by a power-law. (The origin of such a relationship may be electrons in our regime retaining coherent dynamics, and that may not emerge when equilibrating thermal motions are prevalent.) The power-law dependence may be characterized by two parameters, the characteristic electron energy E_0 and the exponent of the power-law dependence on energy E:

$$J(E) = -J_0(1 - E/E_0)^{\alpha}. \tag{6}$$

The index α here designates the steepness of the energy dependence on electrons and it is a measure of the coherence of the electron motion. In other words, the greater α is, the more electrons in coherent motion are contributing to the overall current of the electrons. Thus we may call α the coherence parameter of the electrons. Usually the most energetic electrons are lost from the system and have a minor contribution to the ion acceleration [29–31]. The maximum

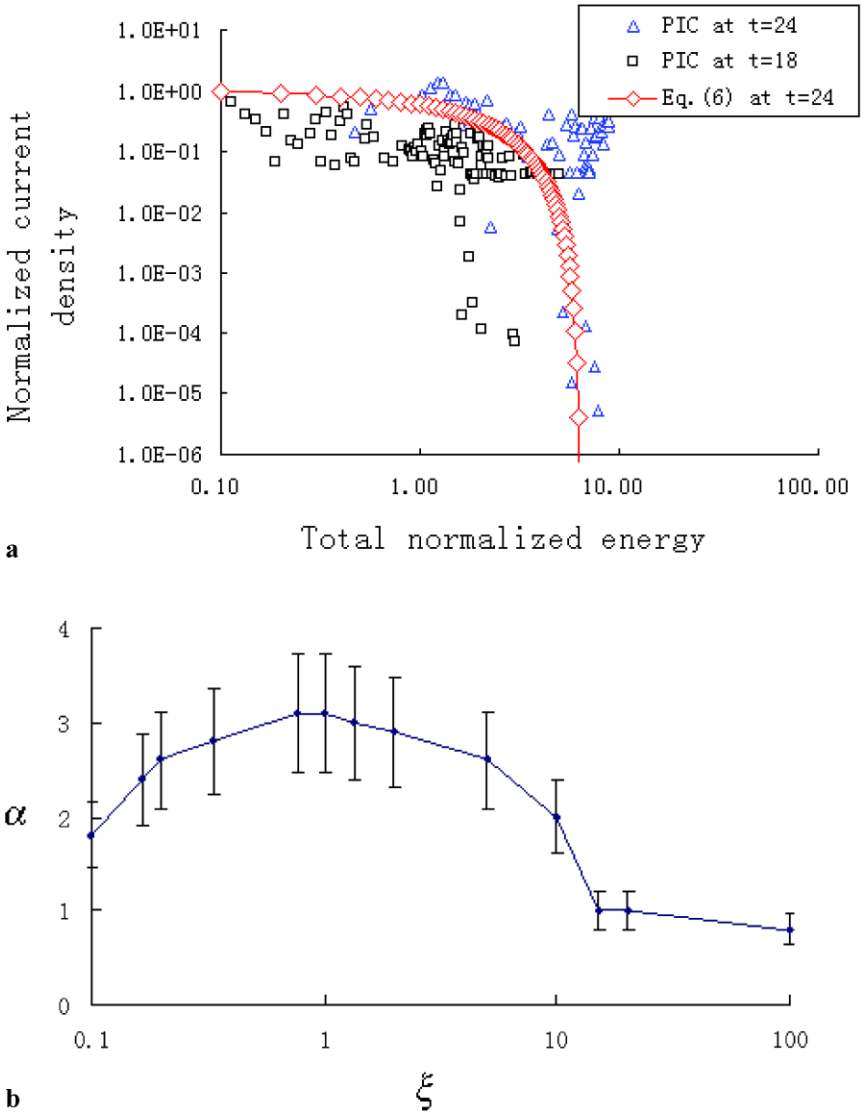

Fig. 2 Backward electron current density $(-J/J_0)$ versus total normalized energy E/m_ec^2. (**a**) The total energy of electrons E and the current density J from 1D3V PIC simulation with $a_0 = 7.2$. Typically the highest transfer of laser energy to the electron and potential energies at the time of laser pulse having transited. In this example, it is around $t = 24$, when we find the values of $E_0 = 6.3$, $\alpha = 3$, which are defined in (6). There are two classes of electrons, the first consisting of those that are quickly ejected with high energies, and the others whose movements are more closely tied with ions. We pay attention to the latter (more discussion in the text later in Sects. 3 and 6 on this). It is noted that because of statistical fluctuations and some ejected high-energy electrons, we encounter relatively large fluctuations away from this curve; (**b**) a plot of the coherence parameter α versus the normalized areal density ξ (keeping $\xi \sim 1$; the simulation box is the same as Fig. 1)

electrostatic potential is smaller than the laser ponderomotive potential or the characteristic electron energy E_0. In the high laser intensity case the relativistic electrons are dominant so that the integral is carried out with the relativistic kinematics as:

$$n_e = \frac{2}{e}\int_0^{V_{\max}} \frac{dJ(\upsilon)/d\upsilon}{\upsilon}\, d\upsilon = \frac{2}{ec}\int_{-e\phi}^{E_0} \frac{dJ(E)}{dE}\, dE$$
$$= -\frac{2J_0}{ec}(1 + e\phi/E_0)^{\alpha} = n_0(1 + e\phi/E_0)^{\alpha}, \qquad (7)$$

where n_0 is the initial plasma density and $J_0 = en_0c/2$.

Fast electrons do not contribute to the acceleration of ions (both proton and carbons). This is why ejected electrons are excluded from measuring the exponent α for $(-J)$ versus E. Figure 2 shows two snapshots of the $J(E)$ curves from the PIC simulations, where theoretical curves are plotted at $t = 18$ and at $t = 24$. Since the maximum laser energy transfer to electrons and the potential energy (the sum of these two) at the time when the laser pulse has just been transmitted through the target, we measure the functional relationship between $-J$ and E. In Fig. 2(a), we superpose this function with the choice of $E_0 = 6.3$, $\alpha = 3$ in the expression of (6). In other words, the characteristic electron energy is reaching 6.3 in units of m_ec^2 at the end of the laser plasma interaction; meanwhile the exponent α remains approximately constant around 3 during this phase of evolution under the optimum ion acceleration condition: $\xi \sim 1$. Figure 2(b) shows α is not very sensitive to ξ varying from 0.2 to 5, while it drops down beyond this range.

3 Self-similar evolution of ion dynamics

The system's evolution needs to be tracked self-consistently with electrons, ions and the interacting electrostatic poten-

tial in time. These consist of a highly nonlinear coupled system of equations. We treat the electrons as discussed in Sect. 2, while we describe the ions in nonrelativistic nonlinear equations in this section.

The nonrelativistic fluid equations are used to describe the response of the ions to the electrostatic field as follows:

$$\frac{\partial n_i}{\partial t} + \frac{\partial}{\partial x}(v_i n_i) = 0, \tag{8}$$

$$\frac{\partial v_i}{\partial t} + v_i \frac{\partial v_i}{\partial x} = -\frac{Qe}{M}\frac{\partial \phi}{\partial x}. \tag{9}$$

where the laser ponderomotive force for ions is neglected.

In order to solve the equations self-consistently, the self-similar condition is invoked by using the fluid equations and electron distribution with the self-similar parameter

$$\zeta = x/(v_0 t), \tag{10}$$

$$v_0 = (Qe\phi_0/M)^{1/2}, \tag{11}$$

$$e\phi_0 = E_0, \tag{12}$$

which is the characteristic electron energy. We introduce the dimensionless parameters

$$U = v_i/v_0, \qquad \Re = n_i/n_0, \qquad \psi = \phi/\phi_0 \tag{13}$$

Equations (8) and (9) now take the form

$$\Re'(U-\zeta) + \Re U' = 0, \tag{14}$$

$$U'(U-\zeta) + \frac{d\psi}{d\Re}\Re' = 0, \tag{15}$$

$$\Re = (1+\psi)^{\alpha}. \tag{16}$$

In deriving (16) the quasineutrality condition is imposed. We already noted in Fig. 2(a) caption that we pay attention to the electron component that moves with the ions. In our simulation, we clearly see that the dynamics of these electrons and ions are tied. (See Fig. 7.) Thus the imposition of quasineutrality is justified.

The conservation of energy is assessed with the boundary condition on the surface of the target:

$$U^2/2 + \psi = 0 \text{ at } \zeta = 0. \tag{17}$$

The solutions to the set of (14)–(16) are

$$\Re = \left\{\frac{\alpha}{(2\alpha+1)^2}\left(\zeta - \sqrt{2(2\alpha+1)}\right)^2\right\}^{\alpha}, \tag{18}$$

$$U = \frac{2\alpha+2}{2\alpha+1}\zeta - \sqrt{\frac{2}{2\alpha+1}}, \tag{19}$$

$$\psi = \frac{\alpha}{(2\alpha+1)^2}\left(\zeta - \sqrt{2\alpha+1}\right)^2 - 1. \tag{20}$$

Equations (18)–(20) also read in usual units

$$n_i = n_0\left\{\frac{\alpha}{(2\alpha+1)^2}\left(\zeta - \sqrt{2(2\alpha+1)}\right)^2\right\}^{\alpha}, \tag{21}$$

$$v_i = \left(\frac{QE_0}{M}\right)^{1/2}\left(\frac{2\alpha+2}{2\alpha+1}\zeta - \sqrt{\frac{2}{2\alpha+1}}\right), \tag{22}$$

$$\phi = \phi_0\frac{\alpha}{(2\alpha+1)^2}\left(\zeta - \sqrt{2\alpha+1}\right)^2 - \phi_0. \tag{23}$$

The maximum energy is assessed when the ion density vanishes. This yields from (18)–(19):

$$\varepsilon_{\max,i} = (2\alpha+1)QE_0. \tag{24}$$

In (24) we see that the ion energy is greater if the coherence parameter of the electrons is greater.

A more general expression for the time-dependent maximum kinetic energy at the ion front from (22) is

$$\varepsilon_{\max,i}(t) = (2\alpha+1)QE_0\left((1+\omega t)^{1/2\alpha+1} - 1\right) \quad (t \le 2\tau). \tag{25}$$

Here τ is the laser pulse duration and ω is the laser frequency. At the beginning the ion energy $\varepsilon_{\max,i}(0) = 0$ and the ion energy approaches infinity as long as the time $t \to \infty$. Normally as the maximum pulse duration of a CPA (Chirped Pulse Amplification) laser is less than pico-seconds, the final ion energy from (25) is only about $\varepsilon_{\max,i}(t = 1\text{ps}) = 2(2\alpha+1)QE_0$. We will discuss the ion energy dependence on the pulse length in detail in Sect. 5.

4 Secondary processes after the laser impingement

When a short laser pulse impinges on a very thin target ($\xi \lesssim 1$), we notice some interesting phenomenon. The laser pulse can partially penetrate the target and enables the electrons to execute dynamic motions still directly tied with the laser rather than thermal motions, as we discussed. In the case of a proton-rich carbon target (C:H = 1:1) it is found that the expelled electrons form a plasma sheet whose density can exceed n_c as Fig. 3(b) shows. Some fraction of the penetrated laser pulse seems to be trapped between the diamond foil and this newly formed electron sheet. This means that the ions are affected not only by the electron energy E_0, but also by the ponderomotive potential Φ_{pt}, which can push electrons less suddenly than the original laser interaction on the target. Thus we need to introduce the characteristic electron energy as

$$\varepsilon_{\max,e} = E_0 + \Phi_{pt}. \tag{26}$$

Because the electron motions are still coherent in the laser field, the electron energy and ponderomotive potential energy can be estimated directly by the laser intensity

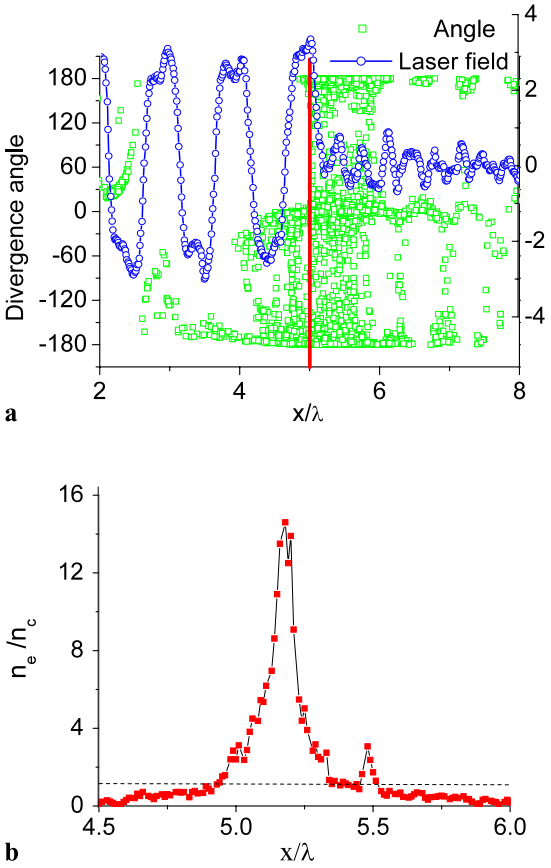

Fig. 3 Snapshot of the laser fields and the display of electron divergence angles at $t = 22$. (**a**) *Blue circles* are the laser field and *green squares* the electron divergence angles. The *vertical bold line* represents the original target position. This shows that the laser pulse is partially transmitted through the target and trapped between the two electron layers; (**b**) Behind the target there is the second electron layer formed due to the laser ponderomotive push (Simulation parameters are the same as Fig. 1)

as [32]:

$$E_0 = m_e c^2(\gamma_p - 1), \qquad \Phi_{pt} = m_e c^2(\gamma_{pt} - 1), \tag{27}$$

$$\gamma_p = \sqrt{1 + (1 - T)a_0^2}, \tag{28}$$

$$\gamma_{pt} = \sqrt{1 + T a_0^2}, \tag{29}$$

where γ_p and γ_{pt} are the electron kinetic energies associated with the incident and transmitted laser pulse. The transmission coefficient T in case of normal incidence can be estimated by [33]

$$T = \frac{1}{1 + (\pi\xi)^2}. \tag{30}$$

$$\varepsilon_{\max,i} = (2\alpha + 1)Q\Big[\Big(\sqrt{(1 - T)a_0^2 + 1} - 1\Big) + \Big(\sqrt{T a_0^2 + 1} - 1\Big)\Big]. \tag{31}$$

We note here that the setup of the electron sheet and consequentially the ponderomotive potential buildup as discussed here no longer occur if the foil is too thick ($\xi \gg 1$). Therefore, in the thick regime the split of two terms as expressed in (26), (27), and (31) do not arise and we should simply take (24). It is also important to notice that in Fig. 3 the transmitted laser pulse has changed its property from that of the incident one, showing a much more minute structure of the field oscillations. Detailed analysis shows that the transmitted laser pulse consists of the fundamental laser frequency as well as those from higher harmonics (HH) of order 2, 3, 4, and so forth to substantial orders. They are both below and above the cutoff frequency of ω_p in the target. (We will report these features of HH in a separate future paper.) It should be emphasized that these transmitted low-order HHs are singular and specific to the organized coherent electron motion directly driven from the electromagnetic fields of the laser penetrating through the thin target. These features have experimentally been observed [34].

When the admixture of ions is predominantly carbon, the dynamics is slightly different and the ion dynamics is basically that of co-moving carbon ions and electrons (discussed in more detail in Sect. 6). In that case we no longer need the second term in (26) and (31). In either case we note that these electrons we take into account move coherently with the laser pulse and subsequently co-move with the ions. This aspect of the dynamics is the most important discrepancy between the TNSA in much thicker targets and the present case.

5 Relativistic transparency and burn-through

We now proceed to consider the cases when the target is thicker ($\xi \gg 1$) than when it is immediately influenced by the laser fields. In this case the laser does not immediately penetrate through the target. When the target becomes so thick that ξ becomes much greater than unity, our model discussed in Sect. 3 becomes less robust, so that we need to remain cautious about its applicability. In this case the interaction process is more complex and we realize that we can delineate at least three stages. The first stage is similar to the situation in Sect. 3. The laser just impinges on the thin surface layer of the dense target. The second stage is after the target begins to expand by the laser interaction primarily in the direction of laser propagation until the plasma becomes relativistically transparent at time t_1. After this relativistic transparency t_1, the plasma expands in all three dimensions. The third stage begins when the plasma becomes underdense at time t_2 till the pulse is over. (Here we have assumed a case where the pulse length is greater than both t_1 and t_2 for the sake of concreteness.)

Now we wish to evaluate the plasma expansion in terms of the two characteristic times t_1 and t_2 as discussed above.

In the solid-density plasma, the skin depth is so small that the ponderomotive force is opposed by the charge-separation force beyond the skin depth. Therefore, the foil expansion in the longitudinal direction may be written as (32), where a laser pulse with the profile $a = a_0 \sin^2(\Omega t)$ is assumed ($\Omega = \frac{\pi}{2\tau}$), thus:

$$\frac{dp}{dt} = -Qe\nabla\phi, \tag{32}$$

$$\nabla\phi \cong \phi_0 a_0 \sin^2(\Omega t)/x, \tag{33}$$

where $a_0 \gg 1$ is assumed and x is the target front. We integrate (32) over dt:

$$\frac{dx}{dt} \cong \frac{Qe\phi_0 a_0[t - \sin(2\Omega t)/2\Omega]}{2Mx}, \tag{34}$$

$$x\,dx = \frac{Qe\phi_0 a_0}{2M}\left(t - \frac{1}{2\Omega}\sin(2\Omega t)\right)dt, \tag{35}$$

$$x^2 - d^2 = \frac{m}{M}\frac{Qc^2 a_0}{3}\Omega^2 t^4. \tag{36}$$

Assuming expansion only in the x direction at the relativistic transparency, the expanded distance x_1 may be evaluated by $x_1 = Nd/\gamma = Nd/\sqrt{a_0^2 + 1}$, $x_1 \gg d$.

Then we obtain:

(1) 1D expansion time t_1

$$t_1 = \left(\frac{M}{m}\frac{3N^2 d^2}{Q\Omega^2 c^2 a_0^3}\right)^{1/4} = \left(\frac{12}{\pi^2}\frac{M}{Qmc^2}\frac{N^2 d^2}{a_0^3}\tau^2\right)^{1/4}$$

$$\cong \left(\frac{12}{\pi^2}\right)^{1/4}\frac{N^{1/2}}{a_0^{1/2}}(\tau d/C_s)^{1/2}. \tag{37}$$

Here $C_s \cong (Qmc^2 a_0/M)^{1/2}$. The relativistic transparency time t_1 in (37) is in the ball park of the geometrical mean of the laser pulse length τ and the traverse time over the target by the sound speed. During this period, the laser pulse penetration is limited as expressed by the transmission coefficient (30). Thus when we integrate the impact on the electron energy at the rear surface of the target to evaluate E_0, we need to incorporate this effect. We have

$$\bar{E}_0(t_1) = m_e c^2 \int_0^{t_1} \left(\sqrt{T(t')a^2(t') + 1} - 1\right)\frac{dt'}{t_1}. \tag{38}$$

$$\varepsilon_{\max,i}(t_1) = (2\alpha + 1)Q\bar{E}_0(t_1)\left((1 + \omega t_1)^{1/2\alpha+1} - 1\right). \tag{39}$$

This integral I in (38) may be evaluated if we split this into two pieces, the contributions $I = I_1 + I_2$ arising from $t = 0, t_1 - \Delta t_1$ and that from $t = t_1 - \Delta t_1, t_1$, where $Nc\Delta t_1/(\lambda a_0) = 1$. The first term may be evaluated as

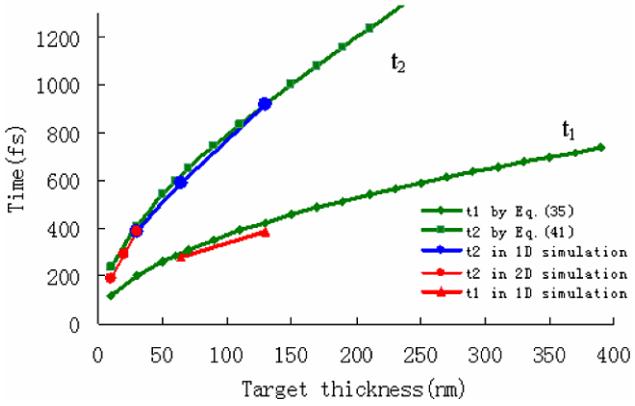

Fig. 4 The relativistic transparency time t_1 and the burn-through time t_2 as a function of the target thickness. We compare our theory with 1D and 2D simulations [36]. (In the simulations $a_0 = 20$, $\lambda = 1$ μm, the FWHM pulse duration $\tau = 700$ fs, the plasma with an initial density of $n_e \cong 800 n_c$ consists of 2 ion species (C^{6+} and H^+))

$$I_1 = m_e c^2 \int_0^{t_1 - \Delta t_1} \left(\sqrt{T(t')a^2(t') + 1} - 1\right)\frac{dt'}{t_1}$$

$$\cong m_e c^2 \frac{\overline{a^2(t_1 - \Delta t_1)}}{\pi(Nd/\lambda)}, \tag{40}$$

while the second integral may be estimated as

$$I_2 = m_e c^2 \int_{t_1 - \Delta t_1}^{t_1} \left(\sqrt{T(t')a^2(t') + 1} - 1\right)\frac{dt'}{t_1}$$

$$\cong m_e c^2 a(t_1)\frac{\lambda}{ct_1}. \tag{41}$$

Both of these terms in (40) and (41) are multiplied by a coefficient typically much smaller than unity over the expression equivalent to (24).

Yin et al. [35] have found that for long pulse irradiation the pulse exhibits an epoch of burn-through or "breakout afterburner" (BOA). This phenomenon is when the laser goes through the target and eventually emerges from the rear end of the target. This corresponds precisely to the second period between t_1 and t_2. We now characterize the physical processes including these phenomena. Beyond time t_1 the plasma is relativistically transparent so that the laser can now interact with the (expanded) target plasma in its entirety. It can also now expand in three dimensions. In Fig. 4 we compare this theoretical value of t_1 and t_2 with simulations. For 3D spherical isotropic expansion, it takes time Δt during which the normalized density reduces from γ to 1:

$$x_2^3 = x_1^3 \gamma. \tag{42}$$

That is

$$dt = \frac{dx}{C_s(t)} = \frac{dx}{(qemc^2 a_0 \sin^2(\Omega t)/M)^{1/2}} = \frac{dx}{C_s \sin(\Omega t)}. \tag{43}$$

We obtain

$$\Delta t = \frac{x_2 - x_1}{C_s}\frac{1}{\sin(\Omega t_1)} = \frac{x_1(\gamma^{1/3}-1)}{C_s}\frac{1}{\sin(\Omega t_1)} = \frac{Nd(\gamma^{1/3}-1)}{\gamma C_s}\frac{1}{\sin(\Omega t_1)}. \quad (44)$$

Now the time t_2 when the plasma becomes underdense is given as

$$t_2 = \Delta t + t_1. \quad (45)$$

In Fig. 4 we compare the theoretical values of t_1 and t_2 with simulations.

Now as we examine the physical situation, we realize that at time t_1 the laser pulse has penetrated the entire target with the relativistic transparency and we may assume that the laser begins to drive the entire plasma electrons from this already expanded target. This process may be once again regarded to evolve in a self-similar fashion. If and when this is the case, the slab of plasma that has been penetrated with the laser may be subject to an expansion in a self-similar treatment similar to what we have done for times before t_1. (A slight difference remains in that we regard our self-similar expansion to be triggered at the laser impingement before t_1, while the second self-similar expansion may be considered to commence at the rear end of the target after t_1.) With this picture we may exercise the same mathematical tracking of the electrons, ions, and their electrostatic field between them assuming the self-similarity initiated at t_1. This process may well be three-dimensional, as we discussed. Here, however, for the sake of simplicity, if we take the same one-dimensional self-similar treatment, we are led to an expression in a closed form for the ion energy gain between time t_1 and t_2 in the case of a laser pulse with the duration longer than the characteristic time t_1, as follows:

$$\varepsilon_{\max,i,\mathrm{BOA}} = (2\alpha+1)Q\bar{E}_0\big(\big(1+\omega(t_2-t_1)\big)^{1/2\alpha+1}-1\big). \quad (46)$$

Here $\bar{E}_0$ is evaluated over the time interval (t_1, t_2) and also note that after t_1 transmission $T = 1$. We have assumed that $t_1 < 2\tau$ and $t_2 < 2\tau$. As we remarked, (43) has been derived for one-dimensional self-similarity. It is thus considered that this would yield an overestimate of energy than a fully three-dimensional solution.

Taking these expressions in (39) and (46), when $t_1, t_2 < 2\tau$, the total ion energy gain can be obtained. In Fig. 5 we plot the total energy gain in the case of carbon ions from this formula as a function of the target thickness, while the contributions from $\varepsilon_{\max,i}(t_1)$ and $\varepsilon_{\max,i,\mathrm{BOA}}$ are also shown. It shows that the BOA term is dominant for thick targets. When this condition $t_1, t_2 < 2\tau$ is not fulfilled, an appropriate corresponding modification for energy is due.

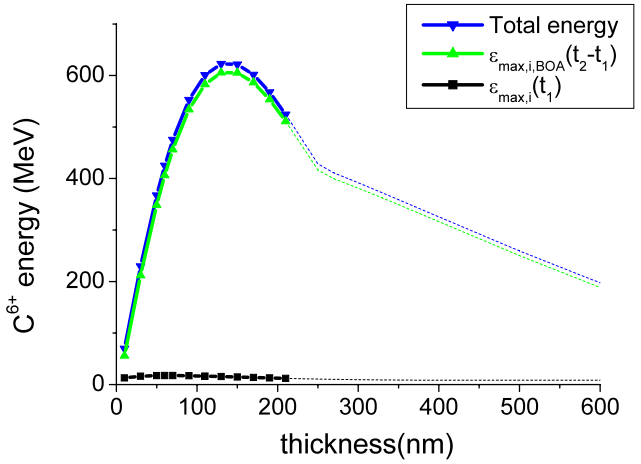

Fig. 5 C^{6+} energy gain estimated from (39) and (46) as a function of the target thickness and with $a \cong 3$. Beyond $\xi > 10$, where α, it is supposed to quickly decrease and the model's predictiveness decreases. (For a given laser pulse length at 700 fs and laser amplitude $a_0 = 20$.) The contribution of the electron energy gain during the breakout afterburner epoch is dominant

It should be further noticed that the laser ponderomotive force can also transversely shove electrons and thereby ions over a time $t_\perp$, while it longitudinally expands the foil plasma at the same time. We evaluate this time $t_\perp$ in the same way as t_1 and it reads

$$t_\perp \cong \left(\frac{24}{\pi^2}\right)^{1/4}(\tau r_0/C_s)^{1/2}. \quad (47)$$

Here r_0 is the laser spot size. In many of our applications it may be that the shoving time $t_\perp$ is greater than the time scales t_2 and t_1 for the nm-scale foils. However, sometimes $t_\perp$ may become smaller than t_1, depending on the parameters.

6 Simulation results

We now discuss more detailed processes regarding cases with the interaction of a short laser pulse. To elucidate these processes, we show 2D simulation results. In the simulation runs nanometer-scale DLC targets are studied. This may be modeled to have a rectangular shaped plasma with an initial density of $n_e \cong 500 n_c$ consisting of 2 ion species (C^{6+} and H^+) in the number ratio of 10:1. In the simulations the Linear Polarized (LP) laser pulse has a Gaussian shape in time with a FWHM of 16 laser cycles, a Gaussian intensity distribution at focus with a FWHM spot size of 4 μm and an intensity of 2.6×10^{19} W/cm^2. The laser wavelength is 0.8 μm. The maximum ion energy is evaluated by (39) and (46). The theoretical prediction of maximum ion energy occurs at around 4.5 nm, which corresponds to the optimum

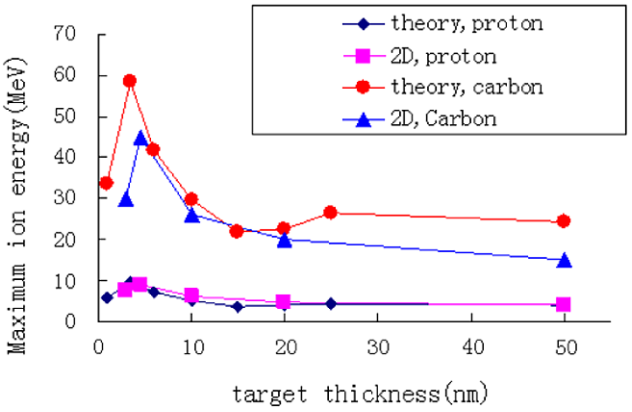

Fig. 6 Maximum proton energy versus the target thickness with the laser intensity kept constant at 2.6×10^{19} W/cm^2 and the pulse length at 50 fs. (Notice that the theoretical ion energy is determined by (39) and (46) and $\alpha \cong 3$)

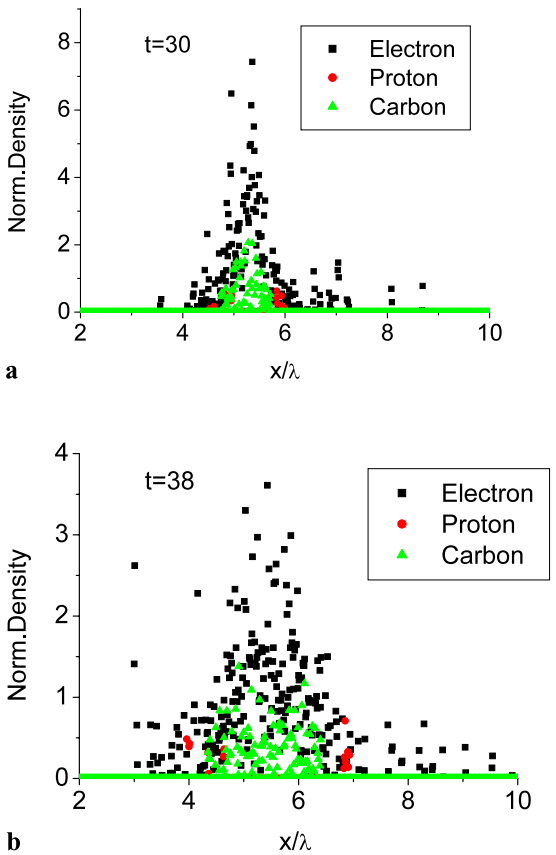

Fig. 7 The substantially co-moving dynamics of electrons and ions after they are driven away by the laser pulse from the original nanometric target. Snapshots of electron, proton, and carbon densities (the DLC target is located at $x = 5\lambda$) at $t = 30$ (*left*) and 38 (*right*). They show two characteristics: the co-movement, and the expansion of the moving target around its center

condition $\xi \sim 1$, as Fig. 6 shows. Our theory well predicts the simulation results.

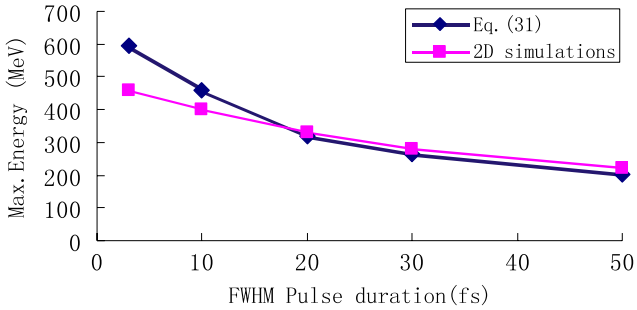

Fig. 8 Maximum proton energy versus pulse duration (at the optimal condition $\xi \sim 1$ and $\alpha \cong 3$). The laser energy is kept constant at 5 J and a_0 is varied from 160 to 40. Since the total energy of the laser is fixed, the shorter the pulse is, the higher the ion energy

Most significant is the dynamics of electrons and ions manifested in the density profiles of electrons and carbon ions on the axis (see Fig. 7). Due to the limited mass contained in the nanometric targets the carbons co-move with electrons, which results in the coincidence of the density peaks of respective species (ions and electrons). This should explain why in a nanometric target we observe substantial adiabatic energy transfer from electrons to ions. In fact what we have observed in the simulations is a remarkably high conversion efficiency from laser energy to ion energy. For proton and carbon ions we find values as high as 1.5% and 9%, respectively, in case of the optimum target thickness $d = 4.5$ nm. Such conversion efficiencies are at least one order of magnitude higher than those in the regime of TNSA with thicker targets [13].

With our predictive theory as a guide, in the second series of runs we try to study the maximum proton energy by varying the different laser pulse duration, while keeping the laser energy constant at 5 J. The LP laser pulse has a Gaussian profile in both the transverse and longitudinal directions with a spot size of 0.8 μm and DLC targets with rich protons (C:H = 1:1) are used in the simulations. Equation (31) is evaluated at $t = \tau$ to compare these simulations. The maximum energy is plotted versus the pulse duration in Fig. 8. This shows that a shorter pulse is more favorable to enhance the proton energy. The obtained ion energies are quite impressive. Again we find that the theory well indicates the expected values of energies that we produced from 2D simulations.

7 Conclusion

The theory developed here for ion acceleration by an UHC laser pulse interacting with an ultrathin (nm-scale) target is a self-similar solution of the coupled electron–ion–electrostatic-field equations. A simple relationship between the accelerated ion energy and that of electrons is found. The theory is valid strictly when such a self-similar situation is

realized. We find that the maximum ion energy is $\varepsilon_{\max,i} = (2\alpha + 1)Q\varepsilon_{\max,e}$. This is equal to $(2\alpha + 1)Q[E_0 + \Phi_{pt}]$, when the target is very thin, $\xi \lesssim 1$. This function increases with the coherence parameter α and the electron energy (the sum of the kinetic energy and the ponderomotive potential). The coefficient α is determined by the exponent of backward current density $(-J)$ versus total electron energy. If the experimental situation is within the theoretical prerogatives, the theory can be used to interpret experimental results. Recent experiments [25, 37, 38] have met this condition. In the optimum ion acceleration condition $\xi \cong 1, \alpha$ is about 3 for the LP. Because of this simplicity, such a formula may be useful in guiding us to anticipate a rough outcome of the experiments. When the foil is ultrathin, we recognize that the electron dynamics remains coherently coupled to the laser field. Thus the energies of electrons and ions are related directly to the laser intensity. In this case the above kinetic energy of electrons and the ponderomotive potential energy may be expressed directly by the laser intensity, leading to a further simplified theoretical expression. The theory seems to be reliably predictive for the expansion in this regime. Our model and simulations show that a few-Joule laser system with UHC and short duration (<50 fs) may provide a proton beam exceeding 250 MeV.

When the laser pulse is longer and/or the target is thicker, the physics becomes more involved since the parameters crucial to the conditions get highly multi-dimensional. To sift through this complex physics, we delineate the physical processes into three time stages, the thin layer interaction, the relativistic transparency (t_1), and the breakout regime (up to t_2). In other words, for a long pulse with the duration larger than the characteristic time t_1, the plasma becomes transparent before the termination of the pulse. It is not without merits to consider an intellectual exercise in which the highly nonlinear coupled system of electrons, ions, and electrostatic fields driven by the intense laser pulse evolves in a self-similar fashion; in such an event an estimate of the ion energy gain may be posted as a guide of experiments (and simulation). In the end what matters most in this regime is the electron energy gain in the breakout afterburner epoch of the laser-electron interaction. Most of the electron energy gain happens during this time. The ion energy gain takes, surprisingly, an analytical form similar to the ultrathin case as a function of electron energy, even though the physical processes to arrive at the electron energy are distinct. The time dependence of the maximum ion energy is also derived, if and when the self-similar evolution is justified. The results are not out of the general behavior of the recent experiments in LANL. It is pertinent to remember that we should remain vigilant about the phenomenological nature of our estimates in these situations and formulaic applications need to be accompanied by caution and wisdom.

When the electron dynamics is slow enough that ions evolve less suddenly, i.e. adiabatically [6, 39], the final energy gain of electrons (and thus that of ions) may not be that of the instantaneous energy dictated by the expression $E_0 = m_e c^2(\sqrt{1 + a_0^2} - 1)$. For example, we have remarked a case of the secondary electron sheet formation that moves together with a class of ions, and a case with a circularly polarized pulse. In the latter, for example, the pulse should cause less electron energy gain than the linearly polarized case. Therefore, the cloud of electrons cannot instantaneously shoot out of the foil, but more gradually leave the target. This renders a possibility that the electron energy is not only proportional to the field strength (proportional to a_0), but also to the time over which electrons are accelerated by $\upsilon \times B$ if this is much longer than the laser period. When an electron substantially co-moves with the laser pulse, this time can be proportional to a_0 or some fraction of it, leading to the proportionality greater than a_0 such as a_0^2. This is beyond the scope of the present paper and is left for a future investigation. We anticipate more results to come in advancing the ion energy by laser acceleration spurred by the current theoretical grip of the physics.

Acknowledgements This work is supported in part by the DFG Cluster of Excellence MAP (Munich-Centre for Advanced Photonics). XQY would like to thank the support from the Alexander von Humboldt Foundation and NSFC (10855001). TT is supported in part by the Special Coordination Fund (SCF) for Promoting Science and Technology commissioned by the Ministry of Education, Culture, Sports, Science and Technology (MEXT) of Japan. We are deeply indebted by the collaboration and discussion with our colleagues F. Krausz, J. Meyer-ter-Vehn, H. Ruhl, A. Henig, D. Jung, D. Kiefer, R. Hoelein, J. Schreiber, J.E. Chen, X.T. He, Z.M. Sheng, Y.T. Li, Z.Y. Guo, J.X. Fang, Y.R. Lu, S. Kawanishi, P. Bolton, S. Bulanov, Y. Fukuda, T. Esirkepov, M. Yamagiwa, M. Tampo, H. Daido, J. Mizuki, M. Abe, M. Murakami, Y. Hishikawa, B.J. Albright, K.J. Bowers, J.C. Fernandez, S. Steinke, M. Schnuerer, T. Sokollik, P.V. Nickles and W. Sandner.

References

1. V.I. Veksler, in *CERN Symposium on High Energy Accelerators and Pion Physics* (CERN, Geneva, 1956), p. 80
2. G. Budker, in *CERN Symposium on High Energy Accelerators and Pion Physics* (CERN, Geneva, 1956), p. 68
3. N. Rostoker, M. Reiser, *Collective Methods of Acceleration* (Harwood Academic, London, 1978)
4. M. Reiser, *Theory and Design of Changed Particle Beams* (Wiley, New York, 1994)
5. S. Humphrey, *Charged Particle Beams* (Wiley, New York, 1990)
6. S. Pastuszka, U. Schramm, M. Geisler, C. Broude, R. Grimm, D. Habs, J. Kenntner, H. Miesner, T. Schuessler, D. Schwalm, A. Wolf, Nucl. Instrum. Methods Phys. Res. A **369**, 11 (1996)
7. S. Chu, Science **253**, 861 (1991)
8. F. Mako, T. Tajima, Phys. Fluids **27**, 1815 (1984)
9. T. Tajima, F. Mako, Phys. Fluids **21**, 1459 (1978)
10. E.L. Clark, K. Krushelnick, J.R. Davies, M. Zepf, M. Tatarakis, F.N. Beg, A. Machacek, P.A. Norreys, M.I.K. Santala, I. Watts, A.E. Dangor, Phys. Rev. Lett. **84**, 670 (2000)

11. A. Maksimchuk, S. Gu, K. Flippo, D. Umstadter, V.Yu. Bychenkov, Phys. Rev. Lett. **84**, 4108 (2000)
12. R.A. Snavely, M.H. Key, S.P. Hatchett, T.E. Cowan, M. Roth, T.W. Phillips, M.A. Stoyer, E.A. Henry, T.C. Sangster, M.S. Singh, S.C. Wilks, A. MacKinnon, A. Offenberger, D.M. Pennington, K. Yasuike, A.B. Langdon, B.F. Lasinski, J. Johnson, M.D. Perry, E.M. Campbell, Phys. Rev. Lett. **85**, 2945 (2000)
13. J. Fuchs, P. Antici, E. D'humières, E. Lefebvre, M. Borghesi, E. Brambrink, C.A. Cecchetti, M. Kaluza, V. Malka, M. Manclossi, S. Meyroneinc, P. Mora, J. Schreiber, T. Toncian, H. Pépin, P. Audebert, Nat. Phys. **2**, 48 (2006). (see review of various early experiments)
14. A. Andreev, A. Levy, T. Ceccotti, C. Thaury, K. Platonov, R.A. Loch, Ph. Martin, Phys. Rev. Lett. **101**, 155002 (2008)
15. A.A. Andreev, S. Steinke, T. Sokollik, M. Schnürer, S. Ter Avetsiyan, K.Y. Platonov, P.V. Nickles, Phys. Plasmas **16**, 013103 (2009)
16. D. Neely, P. Foster, A. Robinson, F. Lindau, O. Lundh, A. Persson, C.-G. Wahlström, P. McKenna, Appl. Phys. Lett. **89**, 021502 (2006)
17. T. Ceccotti, A. Lévy, H. Popescu, F. Réau, P. D'Oliveira, P. Monot, J.P. Geindre, E. Lefebvre, Ph. Martin, Phys. Rev. Lett. **99**, 185002 (2007)
18. E. d'Humières, E. Lefebvre, L. Gremillet, V. Malka, Phys. Plasmas **12**, 062704 (2005)
19. T. Esirkepov, M. Yamagiwa, T. Tajima, Phys. Rev. Lett. **96**, 105001 (2006)
20. K. Matsukado, T. Esirkepov, K. Kinoshita, H. Daido, T. Utsumi, Z. Li, A. Fukumi, Y. Hayashi, S. Orimo, M. Nishiuchi, S.V. Bulanov, T. Tajima, A. Noda, Y. Iwashita, T. Shirai, T. Takeuchi, S. Nakamura, A. Yamazaki, M. Ikegami, T. Mihara, A. Morita, M. Uesaka, K. Yoshii, T. Watanabe, T. Hosokai, A. Zhidkov, A. Ogata, Y. Wada, T. Kubota, Phys. Rev. Lett. **91**, 215001 (2003)
21. X.Q. Yan, C. Lin, Z.M. Sheng, Z.Y. Guo, B.C. Liu, Y.R. Lu, J.X. Fang, J.E. Chen, Phys. Rev. Lett. **100**, 135003 (2008)
22. B.C. Liu, Z.H. He, X.Q. Yan, Z.M. Sheng, Z.Y. Guo, Y.R. Lu, J.E. Chen, IEEE Trans. Plasma Sci. **36**(4), 1854– 1856 (2008)
23. X.Q. Yan, B.C. Liu, Z.H. He, Z.M. Sheng, Z.Y. Guo, Y.R. Lu, J.X. Fang, J.E. Chen, Chin. Phys. Lett. **25**(9), 3330–3333 (2008)
24. S.G. Rykovanov, J. Schreiber, J. Meyer-ter-Vehn, C. Bellei, A. Henig, H.C. Wu, M. Geissler, New J. Phys. **10**, 113005 (2008)
25. S. Steinke, A. Henig, M. Schnuerer, T. Sokollik, P.V. Nickles, D. Jung, D. Kiefer, J. Schreiber, T. Tajima, X.Q. Yan, J. Meyer-ter-Vehn, M. Hegelich, W. Sandner, D. Habs, Phys. Rev. Lett. (2009, submitted)
26. P. Mora, Phys. Rev. Lett. **90**, 185002 (2003)
27. M. Passoni, V.T. Tikhonchuk, M. Lontano, V.Yu. Bychenkov, Phys. Rev. E **69**, 026411 (2004)
28. J. Schreiber, F. Bell, F. Grüner, U. Schramm, M. Geissler, M. Schnürer, S. Ter-Avetisyan, B.M. Hegelich, J. Cobble, E. Brambrink, J. Fuchs, P. Audebert, D. Habs, Phys. Rev. Lett. **97**, 045005 (2006)
29. T.E. Cowan, M. Roth, J. Johnson, C. Brown, M. Christl, W. Fountain, S. Hatchett, E.A. Henry, A.W. Hunt, M.H. Key, A. MacKinnon, T. Parnell, D.M. Pennington, M.D. Perry, T.W. Phillips, T.C. Sangster, M. Singh, R. Snavely, M. Stoyer, Y. Takahashi, Nucl. Instrum. Methods Phys. Res. A **455**, 130 (2000)
30. M. Allen, Y. Sentoku, P. Audebert, A. Blazevic, T. Cowan, J. Fuchs, J.C. Gauthier, M. Geissel, M. Hegelich, S. Karsch, E. Morse, P.K. Patel, M. Roth, Phys. Plasmas **10**, 3283 (2003)
31. S. Kar, K. Markey, P.T. Simpson, C. Bellei, J.S. Green, S.R. Nagel, S. Kneip, D.C. Carroll, B. Dromey, L. Willingale, E.L. Clark, P. McKenna, Z. Najmudin, K. Krushelnick, P. Norreys, R.J. Clarke, D. Neely, M. Borghesi, M. Zepf, Phys. Rev. Lett. **100**, 105004 (2008)
32. S.C. Wilks, W.L. Kruer, M. Tabak, A.B. Langdon, Phys. Rev. Lett. **69**, 1383 (1992)
33. V.A. Vshivkov, N.M. Naumova, F. Pegoraro, S.V. Bulanov, Phys. Plasmas **5**, 2727 (1998)
34. U. Teubner, K. Eidmann, U. Wagner, U. Andiel, F. Pisani, G.D. Tsakiris, K. Witte, J. Meyer-ter-Vehn, T. Schlegel, E. Förster, Phys. Rev. Lett. **92**, 185001 (2004)
35. L. Yin, B.J. Albright, B.M. Hegelich, K.J. Bowers, K.A. Flippo, T.J.T. Kwan, J.C. Fernández, Phys. Plasmas **14**, 056706 (2007)
36. M. Hegelich, L. Yin, Private communications
37. A. Henig, D. Kiefer, K. Markey, D.C. Gautier, K.A. Flippo, S. Leitzring, R.P. Jphnson, L. Yin, B.J. Albright, K.J. Bowers, J.C. Fernandez, S.G. Rykovanov, H.C. Wu, M. Zepf, D. Jung, V.K. Liechtenstein, J. Schreiber, D. Habs, B.M. Hegelich, Phys. Rev. Lett. **103**, 045002 (2009)
38. D. Kiefer, A. Henig, D. Jung, D.C. Gautier, K.A. Flippo, S.A. Gaillard, S. Letzring, R.P. Johnson, T. Shimada, J.C. Fernandez, J. Schreiber, D. Habs, B.M. Hegelich, Eur. Phys. J. D 00199 (2009)
39. M. Murakami, Y. Hishikawa, S. Miyajima, Y. Okazaki, K.L. Sutherland, M. Abe, S.V. Bulanov, H. Daido, T.Zh. Esirkepov, J. Koga, M. Yamagiwa, T. Tajima, in *First International Symposium on Laser-Driven Relativistic Plasmas Applied to Science, Industry and Medicine*, ed. by S.V. Bulanov, H. Daido. AIP Conference Proceedings (AIP, New York, 2008), p. 275